

A *Suzaku* view of IGR J16393–4643

Nazma Islam,^{1,2★} Chandreyee Maitra,³ Pragati Pradhan^{4,5} and Biswajit Paul¹

¹Raman Research Institute, Sadashivnagar, Bangalore 560080, India

²Joint Astronomy Programme, Indian Institute of Science, Bangalore 560012, India

³Laboratoire AIM, CEA–IRFU/CNRS/Université Paris Diderot, Service d’Astrophysique, CEA Saclay, F-91191 Gif sur Yvette, France

⁴St Joseph’s College, Singamari, Darjeeling 734104, West Bengal, India

⁵North Bengal University, Raja Rammohanpur, Darjeeling 734013, West Bengal, India

Accepted 2014 November 11. Received 2014 November 11; in original form 2014 September 22

ABSTRACT

The pulsar IGR J16393–4643 belongs to a class of highly absorbed supergiant high-mass X-ray binaries (HMXBs), characterized by a very high column density of absorbing matter. We present the results of simultaneous broad-band pulsation and spectrum analysis from a 44-ks *Suzaku* observation of the source. The orbital intensity profile created with the *Swift* Burst Alert Telescope (*Swift*–BAT) light curve shows an indication of IGR J16393–4643 being an eclipsing system with a short eclipse semi-angle $\theta_E \sim 17^\circ$. For a supergiant companion star with a $20-R_\odot$ radius, this implies an inclination of the orbital plane in the range 39° – 57° , whereas for a main-sequence B star as the companion with a $10-R_\odot$ radius, the inclination of the orbital plane is in the range 60° – 77° . Pulse profiles created for different energy bands have complex morphology, which shows some energy dependence and increases in pulse fraction with energy. We have also investigated broad-band spectral characteristics, phase-averaged spectra and resolving the pulse phase into peak and trough phases. The phase-averaged spectrum has a very high $N_H (\sim 3 \times 10^{23} \text{ cm}^{-2})$ and is described by a power law ($\Gamma \sim 0.9$) with a high-energy cut-off above 20 keV. We find a change in the spectral index in the peak and trough phases, implying an underlying change in the source spectrum.

Key words: stars: neutron – X-rays: binaries – X-rays: individual: IGR J16393–4643 – X-rays: stars .

1 INTRODUCTION

Supergiant high-mass X-ray binaries (HMXBs) account for one-third of the Galactic HMXB population. These compact objects have early-type supergiant stars as companions and accretion onto the compact object occurs via a stellar wind or Roche-lobe overflow. They are subdivided into Roche-lobe-filling supergiants with short spin periods and underfilled Roche-lobe supergiants with longer spin periods (Jenke et al. 2012). A majority of supergiant HMXBs are persistent sources. Some of the supergiant HMXBs, called highly absorbed supergiant HMXBs, have very strong absorption with column density of absorbing matter $N_H \sim 10^{23} \text{ cm}^{-2}$.

IGR J16393–4643 belongs to the increasing class of heavily absorbed HMXBs detected by the *INTErnational Gamma-Ray Astrophysics Laboratory* (*INTEGRAL*) survey of the Galactic plane, which are mainly concentrated in the spiral arms. It was first discovered with the *Advanced Satellite for Cosmology and Astrophysics* (*ASCA*) observatory during a survey of the Galactic plane (Sugizaki et al. 2001) and was named AX J1639.0–4642. It has a spin period

of ~ 910 s and a 4.2-d orbital period (Bodaghee et al. 2006; Corbet et al. 2010) and occupies a unique position near the top edge of underfilled Roche-lobe supergiant systems in the Corbet diagram (Jenke et al. 2012). Due to the lack of detailed studies of such systems, IGR J16393–4643 makes an interesting candidate with which to study the timing and spectral properties of short-orbital-period and long-spin-period supergiant systems.

The X-ray spectrum of the pulsar is characterized by a highly absorbed power law with an exponential cut-off, along with Fe fluorescence lines (Lutovinov et al. 2005; Bodaghee et al. 2006). The strong absorption, of order $\sim 10^{23} \text{ cm}^{-2}$, is evidence of a dense circumstellar environment surrounding the pulsar. Previous observations with *XMM–Newton* indicate the presence of a soft excess in the spectrum, which could be due to X-ray scattering by the stellar wind (Bodaghee et al. 2006).

Here, we present simultaneous broad-band pulse profiles and spectral characteristics of the pulsar IGR J16393–4643 obtained from a *Suzaku* observation. We also present results from the orbital intensity profile analysis of IGR J16393–4643 using *Swift* Burst Alert Telescope (*Swift*–BAT) light curves. Energy-resolved pulse profiles are created for the first time for this source. The broad-band spectral characteristics are studied for the phase-averaged case, as

★ E-mail: nazma@rri.res.in

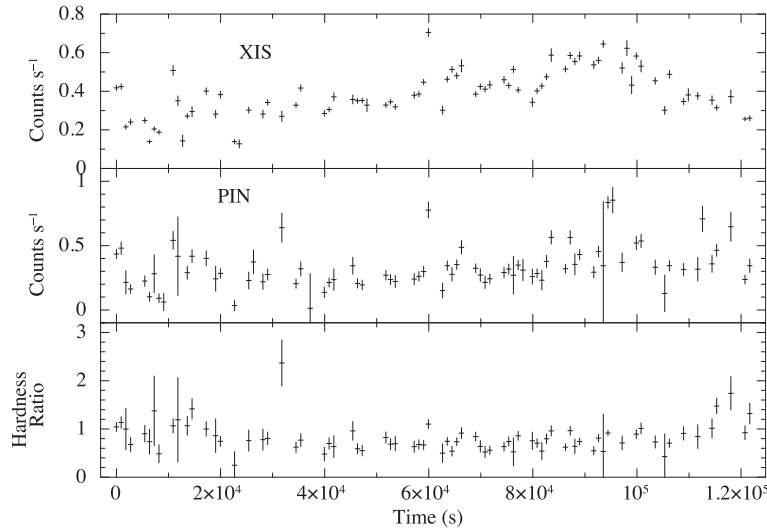


Figure 1. The light curve of IGR J16393–4643 binned at the pulse period of 908 s in the 0.3–12 keV XIS energy band (top panel) and 12–50 keV PIN energy band (middle panel) and the hardness ratio of the count rates in PIN and XIS (bottom panel) are shown.

well as on resolving the pulse phase into peak and trough phases. These results provide valuable insights into the nature of underfilled Roche-lobe supergiant systems.

2 OBSERVATIONS AND DATA ANALYSIS

Suzaku is the fifth Japanese X-ray astronomy satellite, launched in 2005 July. It consists of two sets of co-aligned scientific instruments: the X-ray Imaging Spectrometer (XIS), operating in the energy range 0.2–12 keV, and the Hard X-ray Detector (HXD), operating in the energy range 10–600 keV. The XIS consists of three front-illuminated CCD detectors and one back-illuminated CCD detector (Koyama et al. 2007), out of which three CCDs, XIS0, XIS1 and XIS3, are currently operational. The HXD consists of silicon PIN diodes operating in energy range 10–70 keV and GSO crystal scintillators extending the energy range to 600 keV (Takahashi et al. 2007).

IGR J16393–4643 was observed with *Suzaku* during 2010 March 12 (ObsId: 404056010) with a useful exposure time of ~ 44 ks over a span of about 120 ks. The observations were carried out at the ‘XIS nominal’ pointing position and the XIS was operated in ‘standard’ data mode in the ‘Normal window’ option, having a time resolution of 8 s. For both the XIS and HXD data, we have used the filtered cleaned event files, which are obtained using the pre-determined screening criteria described in the *Suzaku* ABC guide.¹

The XIS light curves and spectra were extracted from the cleaned event files by selecting circular regions of 3 arcmin around the source centroid. The background light curves and spectra were extracted by selecting circular regions of the same size away from the source centroid. For the HXD/PIN background, simulated ‘tuned’ non-X-ray background event files (NXB) corresponding to the month and year of the observation were used to estimate the non-X-ray background.² The cosmic X-ray background was simulated as suggested by the instrument team, with appropriate normalizations and response files.³ The response files for XIS were created

using CALDB ‘20140211’, while for HXD/PIN the response files were obtained from the *Suzaku* Guest Observer Facility.⁴

3 TIMING ANALYSIS

For the timing analysis of the source, we have applied barycentric corrections to the event data files using the `FTOOLS` task ‘aebarycen’. Light curves with time resolutions of 1 and 8 s were extracted from HXD/PIN (12–50 keV) and XIS (0.3–12 keV), respectively. Fig. 1 shows the light curves binned with a time bin of 908 s, i.e. at the pulsar spin period, in XIS and PIN along with the hardness ratio. The count rate in XIS and PIN increases gradually from the start of the observation up to 100 ks by a factor of ~ 2 and then decreases by a similar factor until the end of the observation (also see the second and third panels in Fig. 2). The hardness ratio remains constant throughout the observation.

3.1 Orbital intensity profile analysis

We have used the long-term light curve of IGR J16393–4643 in the 15–50 keV *Swift*–BAT energy band to estimate the orbital period of the system ($P_{\text{orb}} = 366$ 150 s; consistent with Corbet et al. 2010). We then folded the XIS and PIN light curves with the *Swift*–BAT light curves, to investigate the orbital phase of the *Suzaku* observation. The minimum of the orbital intensity profile is taken as orbital phase zero, corresponding to epoch MJD 53417.955. Fig. 2 shows an indication that the system is an eclipsing binary, which was also reported previously by Corbet & Krimm (2013). The eclipse duration is short, with eclipse semi-angle $\theta_E \sim 17^\circ$. The *Suzaku* observations were carried out roughly from orbital phase 0.55–0.9, i.e. prior to going into eclipse. As seen in Fig. 2, the count rate in XIS and PIN increases by a factor of ~ 2 during orbital phase ~ 0.65 –0.8 and then decreases again until the end of the observation. The orbital intensity profile created with *Swift*–BAT is averaged over many orbital cycles, whereas the orbital intensity profiles created with XIS and PIN show variability on sub-orbital

¹ <http://heasarc.nasa.gov/docs/suzaku/analysis/abc/node9.html>

² <http://heasarc.gsfc.nasa.gov/docs/suzaku/analysis/pinbgd.html>

³ http://heasarc.gsfc.nasa.gov/docs/suzaku/analysis/pin_cxb.html

⁴ <http://heasarc.gsfc.nasa.gov/docs/heasarc/caldb/suzaku>

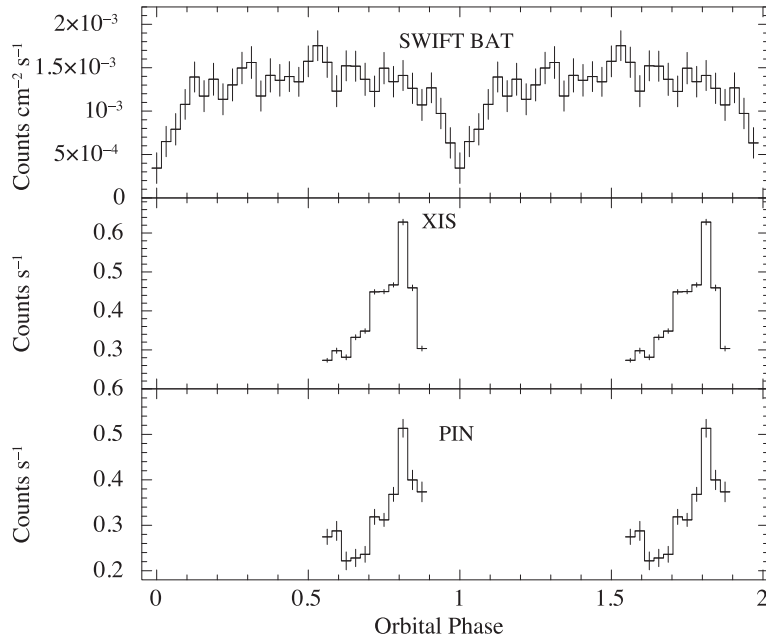


Figure 2. The light curve of *Swift*-BAT, XIS and PIN folded with the orbital period ($P_{\text{orb}} = 366\,150$ s) of IGR J16393–4643. Orbital phase zero corresponds to the eclipse at epoch MJD 53417.955.

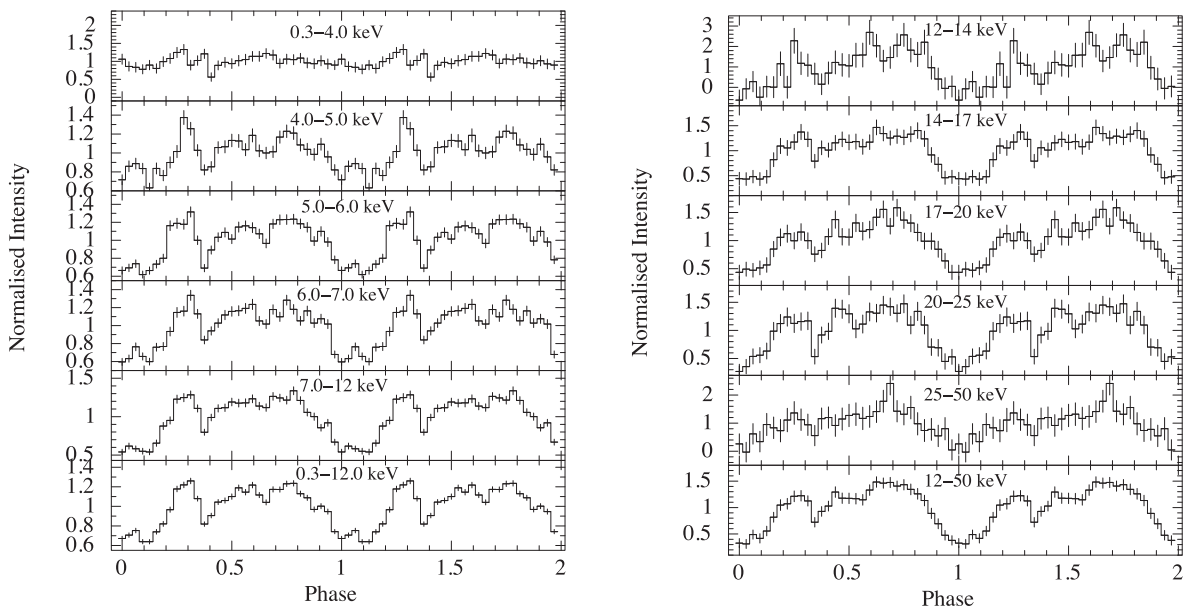


Figure 3. Energy-resolved pulse profiles of IGR J16393–4643 folded with a period of 908.79 s for XIS energy bands (left panel) and PIN energy bands (right panel). The epoch is chosen such that the pulse minima occur at phase 0.0 in the PIN 12–50 keV energy band.

time-scales, similar to that seen in OAO 1657–415 (Pradhan et al. 2014).

3.2 Energy-resolved pulse profiles

We have searched for pulsations in the light curves by applying pulse-folding and the χ^2 maximization technique and the pulse period was found to be 908.79 ± 0.01 s. We then created energy-resolved pulse profiles by folding light curves extracted in different energy bands with the pulse period. Light curves from XIS0, XIS1 and XIS3 were added together to create the pulse profiles in the XIS energy band 0.3–12 keV and sub-bands within. From Fig. 3,

we see that the pulse profiles have a complex morphology with some energy dependence, which was also seen with *XMM-Newton* (Bodaghee et al. 2006) and the *Rossi X-ray Timing Explorer* (RXTE) Proportional Counter Array (PCA) (Thompson et al. 2006), but the broad-band nature of the pulse profiles is highlighted in this *Suzaku* observation. Due to the presence of a high column density of absorbing matter, very few photons are detected below 4 keV. The epoch for creation of the pulse profiles is adjusted to make the minima appear at phase zero in the PIN 12–50 keV energy band. The pulse minima are seen to become deeper at higher energies. A phase lag is seen in the energy-resolved pulse profiles in the two XIS energy bands compared with the PIN energy bands; this is shown

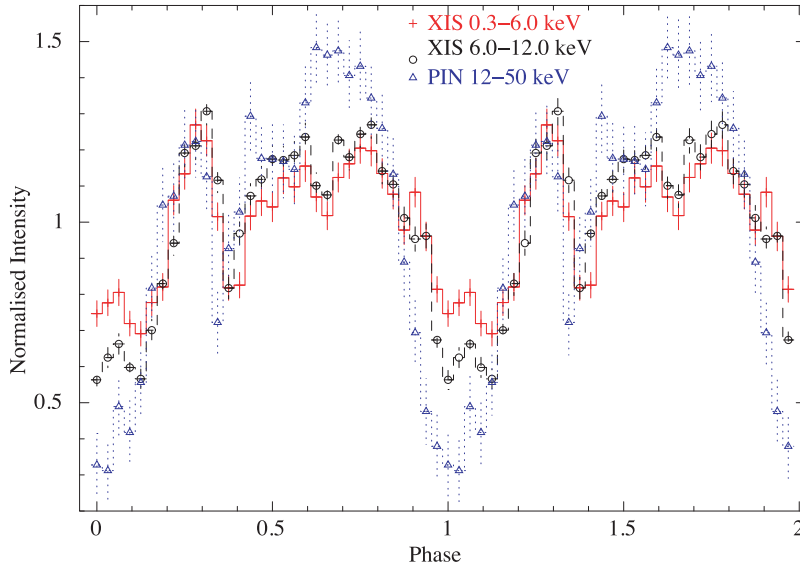


Figure 4. Overlaid pulse profiles created in XIS energy bands 0.3–6.0 and 6–12 keV and in PIN energy band 12–50 keV, showing an indication of phase lag.

in Fig. 4 for pulse profiles created in XIS energy bands 0.3–6.0 and 6–12 keV and in PIN energy band 12–50 keV.

4 SPECTRAL ANALYSIS

4.1 Pulse phase averaged spectrum

We have performed pulse-phase-averaged spectral analysis of IGR J16393–4643 using spectra from three XIS and PIN. The energy range chosen for spectral fitting was 3.0–10.0 keV for XIS, since there were hardly any photons below 3.0 keV. For PIN, the energy range chosen was from 15–50 keV. The XIS spectra were rebinned by a factor of 12 up to 5 keV, by a factor of 6 from 5–7 keV and again by a factor of 12 from 7–10 keV. The PIN spectra were rebinned by a factor of 2 up to 22 keV, by a factor of 8 from 22–45 keV and by a factor of 12 for the remainder. The spectral fitting was performed with `xSPEC` 12.8.1. To fit the continuum spectra, we have tried several standard continuum models used for HMXB pulsars, like the cut-off power law (CUTOFFPL), power law with high-energy cut-off (HIGHECUT: White, Swank & Holt 1983), power law with a Fermi–Dirac cut-off (FDCUT: Tanaka 1986) and negative and positive power-law exponential (NPEX: Mihara 1995). The power law with HIGHECUT and power law with FDCUT spectral models provided the best fits to the phase-averaged spectrum with physically acceptable parameter values; henceforth, we report the results from these two spectral models.

We fitted the spectra simultaneously with all the parameters tied, except the relative normalizations of the instruments, which were kept free. A 6.4-keV Fe $K\alpha$ line was also found in the spectra, which was modelled by a Gaussian emission line. The 7.1-keV $K\beta$ line detected in the spectra from the *XMM–Newton* observation (Bodaghee et al. 2006) was marginally detected here, with a 90 per cent upper limit on the line flux of 2×10^{-5} photon $\text{cm}^{-2} \text{s}^{-1}$ and equivalent width of 33 eV, consistent with the upper limits quoted for the *XMM–Newton* observation (6×10^{-5} photon $\text{cm}^{-2} \text{s}^{-1}$ and 120 eV respectively; Bodaghee et al. 2006). The best-fitting parameter values of the phase-averaged spectrum for 90 per cent confidence limits (except for $\sigma_{K\alpha}$ and equivalent width of the Fe line, which are given for 1σ confidence limits) for the two spectral

models, power law with HIGHECUT and power law with FDCUT, are given in Table 1. Fig. 5 shows the best-fitting phase-averaged spectrum using the power law with HIGHECUT and power law with FDCUT models, along with the residuals.

4.2 Pulse phase resolved spectrum

The energy dependence of the pulse fraction as seen in the XIS and PIN energy bands (Figs 3 and 4) indicates a significant change in the spectrum with pulse phase and we investigate this with pulse-phase-resolved spectroscopy at the peak and trough of the pulse profile. The XIS and PIN spectra were binned into two states: a peak phase around the pulse maximum (phase 0.4–0.8) and a trough phase around the pulse minima (phase 0.0–0.2 and 0.9–1.0), similar to the pulse phase definition used in Bodaghee et al. (2006). In the peak phase, as well as the trough phase, the XIS spectra and PIN spectra were rebinned by the same factors used in phase-averaged spectra. To study the changes in spectral parameters in the two pulse phases, we used the same models as in the phase-averaged spectrum. However, the width of the Fe $K\alpha$ line could not be constrained in the peak phase spectra and was fixed to its phase-averaged value. The best-fitting parameter values of the peak and trough phase spectra for 90 per cent confidence limits (except for $\sigma_{K\alpha}$ and equivalent width of the Fe line for both spectral models, which are given for 1σ confidence limits) for the two spectral models power law with HIGHECUT and power law with FDCUT are given in Table 1. Fig. 6 shows the peak and trough phase spectra using power law with HIGHECUT and power law with FDCUT spectral models, along with the residuals. A softening in the spectrum with an increase in Fe equivalent width is noticed during the trough phase.

5 DISCUSSION

5.1 Orbital intensity profile and inclination of the system

The first panel in Fig. 2 is the orbital intensity profile created by folding the long-term light curve of IGR J16393–4643 obtained with *Swift*–BAT in the energy range 15–50 keV, with the orbital period of the system ($P_{\text{orb}} = 366\,150$ s). The orbital intensity profile

Table 1. Best-fitting parameter values for power law with HIGHECUT and power law with FDCUT models for the phase-averaged spectrum as well as the peak-phase and trough-phase spectra. Errors quoted for $\sigma_{K\alpha}$ and the equivalent width of the Gaussian Fe $K\alpha$ line are for 1σ confidence limits, while those for the remaining parameters are for 90 per cent confidence limits.

Parameters	Phase-averaged		Peak phase		Trough phase	
	HIGHECUT	FDCUT	HIGHECUT	FDCUT	HIGHECUT	FDCUT
N_H (10^{22} atom cm^{-2})	26.5 ± 0.8	26.2 ± 0.8	27.4 ± 1.2	27.1 ± 1.2	26.4 ± 1.7	26.0^{+2}_{-3}
Photon index (Γ)	0.91 ± 0.06	$0.86^{+0.07}_{-0.08}$	0.82 ± 0.09	$0.76^{+0.10}_{-0.13}$	1.2 ± 0.1	1.2 ± 0.1
Γ_{norm} (10^{-3} photon cm^{-2} s^{-1})	$3.8^{+0.5}_{-0.4}$	3.5 ± 0.5	$3.7^{+0.8}_{-0.6}$	$3.4^{+0.8}_{-0.6}$	$5.1^{+1.6}_{-1.2}$	$4.7^{+1.8}_{-1.4}$
Cut-off energy (E_C , keV)	20 ± 1	25^{+1}_{-3}	20 ± 1	25^{+2}_{-5}	19^{+6}_{-4}	25^{+4}_{-6}
Fold energy (E_F , keV)	9 ± 1	5 ± 1	9 ± 2	5 ± 2	11^{+5}_{-7}	6 ± 3
$F_{K\alpha}$ (10^{-5} photon cm^{-2} s^{-1})	$3.2^{+0.8}_{-0.7}$	$3.2^{+0.8}_{-0.7}$	3.9 ± 1.1	3.9 ± 1.1	5.1 ± 2.0	$5.2^{+1.9}_{-2.1}$
$\sigma_{K\alpha}$ (keV)	$0.02^{+0.03}_{-0.02}$	$0.02^{+0.03}_{-0.02}$	–	–	$0.13^{+0.05}_{-0.06}$	$0.14^{+0.04}_{-0.06}$
Equivalent width (eV)	46^{+7}_{-6}	46^{+7}_{-6}	47^{+8}_{-8}	48^{+8}_{-8}	99^{+23}_{-22}	102^{+21}_{-25}
Flux (XIS) (0.3–12 keV) (10^{-11} erg cm^{-2} s^{-1})	3.6 ± 0.1	3.5 ± 0.1	4.2 ± 0.1	4.2 ± 0.1	2.5 ± 0.1	2.5 ± 0.1
Flux (PIN) (12–70 keV) (10^{-11} erg cm^{-2} s^{-1})	2.7 ± 0.1	2.6 ± 0.1	3.4 ± 0.2	3.2 ± 0.2	1.6 ± 0.1	1.5 ± 0.2
$\chi^2_{\nu}/\text{d.o.f}$	1.17/296	1.18/296	1.03/280	1.05/281	1.10/289	1.09/289

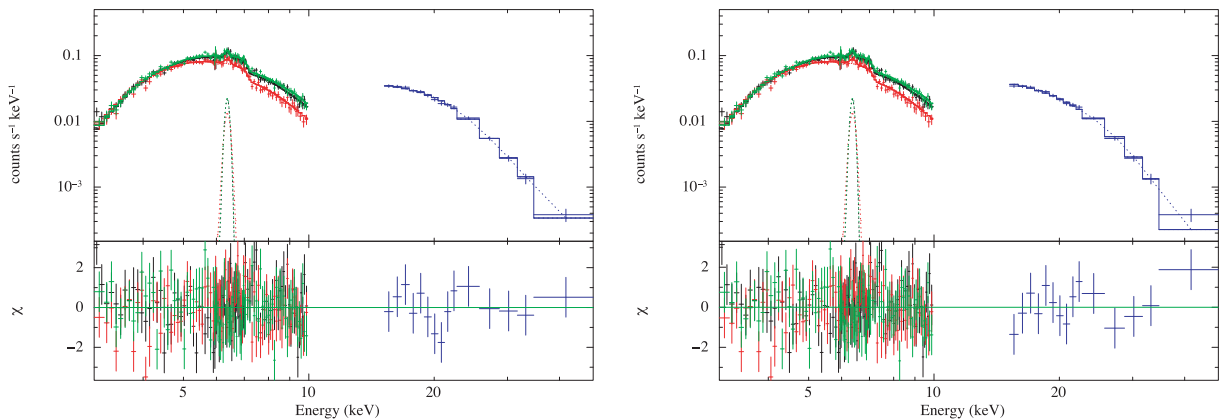


Figure 5. The phase-averaged spectrum of IGR J16393–4643 with the best-fitting models power law with HIGHECUT (left panel) and power law with FDCUT (right panel), along with the contribution of residuals to χ^2 .

shows a narrow eclipse around orbital phase zero, with eclipse semi-angle $\theta_E \sim 17^\circ$. Recent *Chandra* observations of this binary system proposed the optical counterpart to be either a supergiant O9 star with radius $R \sim 20 R_\odot$ or a main-sequence B star with radius $R \sim 10 R_\odot$ (Bodaghee et al. 2012). The short orbital period of the binary system makes it more likely to have a supergiant O9 star as its companion than a main-sequence B star. However, Bodaghee et al. (2012) pointed out that having a supergiant O9 star as a companion would imply a lower limit of distance of 25 kpc to the binary, compared with a distance of 12 kpc for a main-sequence B star.

Supergiant HMXBs like Cen X-3, Vela X-1 and OAO 1657–415 have masses of the companion star in the range $10\text{--}30 M_\odot$ and radii in the range $10\text{--}35 R_\odot$, with a nearly circularized orbit (Rappaport & Joss 1983; van Kerkwijk, van Paradijs & Zuiderwijk 1995; Ash et al. 1999; Mason et al. 2012). Thus, assuming a circular orbit, the separation between the binary components, a , can be expressed as

$$a^3 = \frac{G(M_c + M_{\text{NS}})P_{\text{orb}}^2}{4\pi^2}, \quad (1)$$

where M_{NS} is the mass of the neutron star, which is assumed to be $1.4 M_\odot$, $P_{\text{orb}} = 4.24$ d is the orbital period of the system and M_c is the mass of the supergiant companion star, which is assumed to be in the range $10\text{--}30 M_\odot$.

For an orbital separation a , we then calculated the range of inclination i as a function of the companion star radius R_O given by equation (2) (Rubin et al. 1996):

$$\frac{R_O}{a} = \sqrt{\cos^2(i) + (\sin^2(i) \sin^2(\theta_E))}, \quad (2)$$

where $\theta_E \sim 17^\circ$ is the observed eclipse semi-angle. The upper limit to the companion radius for a given mass is constrained by the Roche-lobe radius R_{Roche} , which is given by equation (3) (Bowers & Deeming 1984; Hill et al. 2005):

$$R_{\text{Roche}} = a \left[0.38 + 0.2 \log \left(\frac{M_c}{M_{\text{NS}}} \right) \right]. \quad (3)$$

Similarly, we carried out the above calculations for the companion as a main-sequence B star having mass in the range $2\text{--}16 M_\odot$ and radius in the range $5\text{--}25 R_\odot$ (Habets & Heintze 1981) and assuming a circular orbit. Fig. 7 is a plot of the range of inclination angles allowed for a given mass of the O9 supergiant companion star and main-sequence B star as a function of its radius, assuming a circular orbit.

For a supergiant companion star radius of $20 R_\odot$, the inclination of the orbital plane of the binary system is in the range $39^\circ\text{--}57^\circ$. For a main-sequence B star of radius $10 R_\odot$, the inclination of the orbital plane of the binary system is in the range $60^\circ\text{--}77^\circ$.

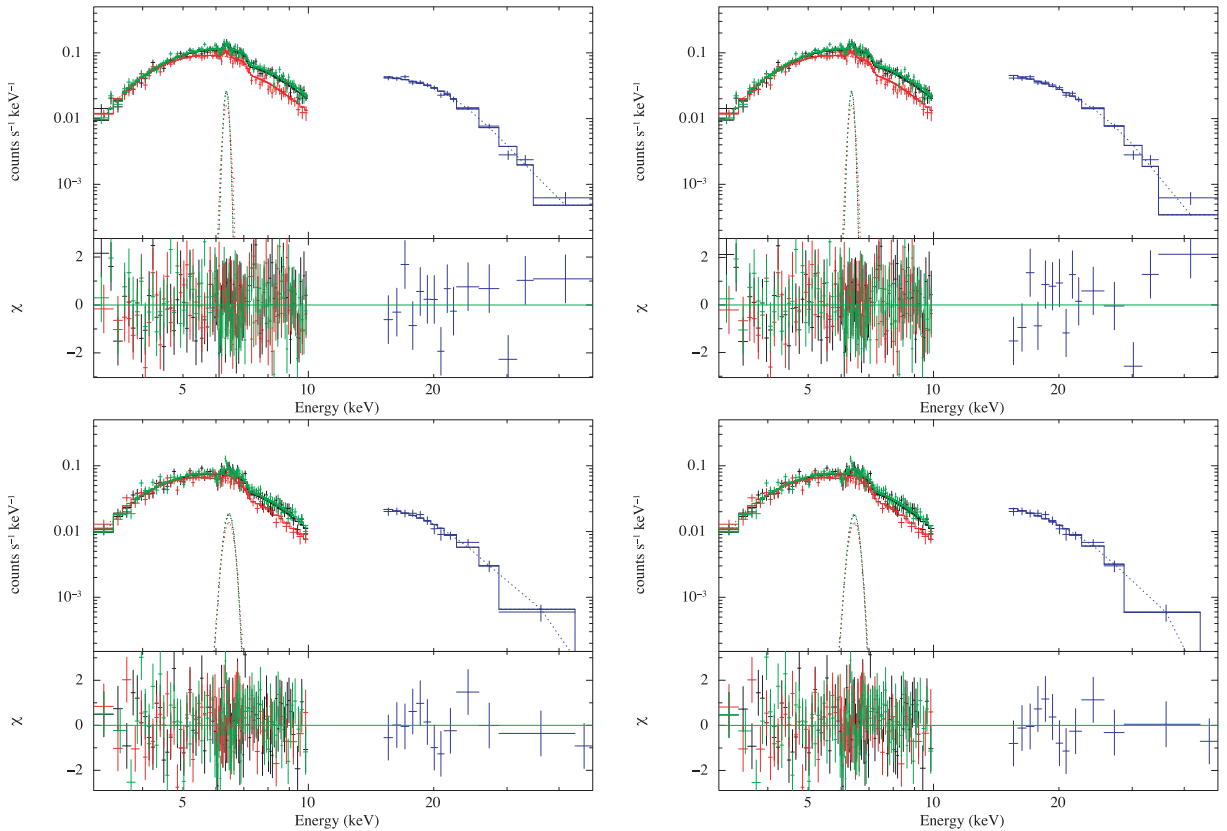


Figure 6. The peak phase spectrum of IGR J16393–4643 using the power law with HIGHECUT model (upper left panel) and power law with FDCUT model (upper right panel), along with the contribution of residuals to χ^2 . The two lower panels show the same for the trough phase.

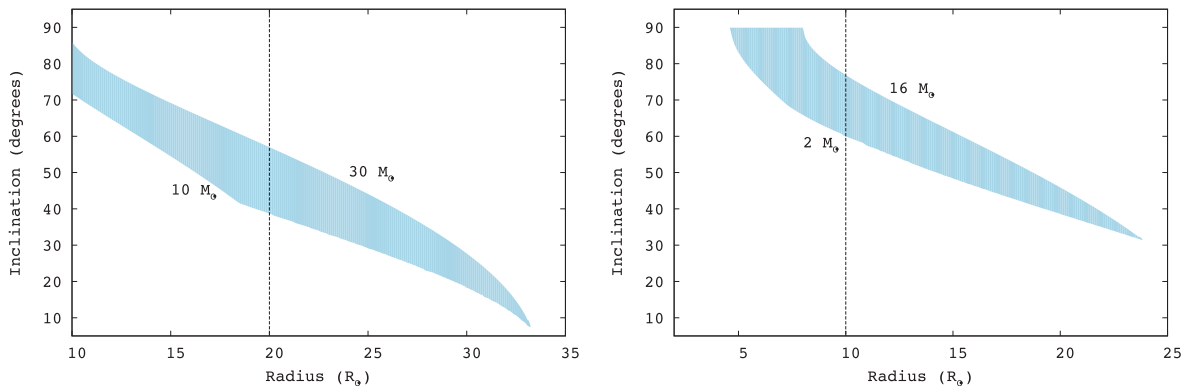


Figure 7. The left panel shows the range of inclination angles allowed for a given mass of the O9 supergiant companion star as a function of its radius, assuming a circular orbit. The right panel shows the range of inclination angles allowed for a given mass of the main-sequence B star as a function of its radius, also assuming a circular orbit. See the text for details. The dotted lines represent the $20\text{-}R_{\odot}$ radius for a supergiant companion and the $10\text{-}R_{\odot}$ radius for a B-type companion (Bodaghee et al. 2012).

5.2 Energy-dependent pulse profiles

Fig. 3 shows the complex double-peaked pulse profiles of IGR J16393–4643 in the *Suzaku* energy sub-bands. The pulse fraction increases with energy, from ~ 33 per cent in the XIS 0.3–12 keV energy band to ~ 65 per cent in the PIN 12–50 keV energy band, which is also seen in many other X-ray pulsars (White et al. 1983; Frontera & Dal Fiume 1989; Nagase 1989). There is a narrow dip present in the pulse profiles at pulse phase ~ 0.35 , which was

also seen in pulse profiles created with the *RXTE* PCA (Thompson et al. 2006) and *XMM-Newton* (Bodaghee et al. 2006). This narrow dip exists even at higher energies, as seen in Figs 3 and 4 for XIS and PIN energy bands. Narrow high-energy dips in the pulse profiles are seen in other X-ray pulsars like GX 1+4 (Naik, Paul & Callanan 2005), EXO 2030+375 (Naik et al. 2013) and A0535+262 (Frontera et al. 1985; Cemiljic & Bulik 1998) and are associated with the intrinsic beaming pattern of the source. From Fig. 4, we see a phase lag of soft photons with respect to hard photons in

the energy-resolved pulse profiles. Such soft phase lags have been observed in millisecond X-ray pulsars (Cui, Morgan & Titarchuk 1998; Ibragimov, Kajava & Poutanen 2011). However, further analysis with respect to the actual cause of phase lag is limited by the statistical quality of the data.

5.3 Phase-resolved spectral characteristics

From the phase-averaged spectral characteristics of IGR J16393–4643 (Table 1 and Fig. 5), we find very high line-of-sight column density of absorbing matter, $\sim 3 \times 10^{23} \text{ cm}^{-2}$. Such a high column density of absorbing matter has been found in previous studies of this system by the *RXTE* PCA (Thompson et al. 2006) and *XMM-Newton* (Bodaghee et al. 2006) and is attributed to the circumstellar environment around the pulsar. The phase-averaged spectrum is described by a power law with spectral index $\Gamma \sim 0.9$ and a high-energy cut-off above 20 keV. The presence of the soft excess detected from the *XMM-Newton* observation (Bodaghee et al. 2006) could not be confirmed in the *Suzaku* observation. Due to the limited statistical quality of this *Suzaku* observation, it is difficult to make an in-depth pulse-phase-resolved spectral analysis.

Instead, the pulse profile is broadly resolved into peak and trough phases and the pulse phase dependence of the spectral properties is studied in these two phase bins (Fig. 6). While the column density is similar in both pulse phases, there is a change in the continuum spectral parameters, which is observed for both spectral models in Table 1. The spectrum is softer at the trough phase and harder at the peak phase, which may be due to additional softer photons near the off-pulse regions. Alternately, this may also imply a deeper and more direct view into the emission region along the magnetic axis at the pulse peak, as would be for the case for a fan beam kind of emission pattern (Pravdo et al. 1976). The cut-off parameters (fold energy E_F and cut-off energy E_C) for both power law with HIGHECUT and power law with FDCUT spectral models, however, remain constant in the two pulse phases. The Fe $K\alpha$ line is present in both phases, with equivalent width higher in the trough phase than in the peak phase. In contrast with the results obtained in Bodaghee et al. (2006) with *XMM-Newton*, which operated in the limited energy band of 0.3–10 keV, there is an underlying change in the source spectrum as a function of pulse phase, which is brought out in this broad-band *Suzaku* observation.

IGR J16393–4643 makes an interesting candidate for detailed pulse-phase-resolved spectroscopy for future X-ray missions with broad-band energy coverage. Such in-depth analysis will help yield a better understanding of the accretion geometry and beaming pattern of underfilled Roche-lobe systems.

ACKNOWLEDGEMENTS

The authors thank an anonymous referee for useful comments. The data used for this work have been obtained through the High Energy Astrophysics Science Archive (HEASARC) Online Service

provided by NASA/GSFC. We have also made use of the public light curves from the *Swift*–BAT site.

REFERENCES

- Ash T. D. C., Reynolds A. P., Roche P., Norton A. J., Still M. D., Morales-Rueda L., 1999, *MNRAS*, 307, 357
- Bodaghee A., Walter R., Zurita Heras J. A., Bird A. J., Courvoisier T. J.-L., Malizia A., Terrier R., Ubertini P., 2006, *A&A*, 447, 1027
- Bodaghee A., Rahoui F., Tomsick J. A., Rodriguez J., 2012, *ApJ*, 751, 113
- Bowers R. L., Deeming T., 1984, *Astrophysics*, Vol. 1, Stars. Jones and Bartlett Publishers, Boston, MA
- Cemeljic M., Bulik T., 1998, *Acta Astron.*, 48, 65
- Corbet R. H. D., Krimm H. A., 2013, *ApJ*, 778, 45
- Corbet R. H. D., Krimm H. A., Barthelmy S. D., Baumgartner W. H., Markwardt C. B., Skinner G. K., Tueller J., 2010, *The Astronomer's Telegram*, 2570, 1
- Cui W., Morgan E. H., Titarchuk L. G., 1998, *ApJ*, 504, L27
- Frontera F., Dal Fiume D., 1989, in Hunt J., Battrick B., eds, *ESA Special Publication Vol. 296, Two Topics in X-Ray Astronomy, Volume 1: X Ray Binaries. Volume 2: AGN and the X Ray Background*, pp. 57–69
- Frontera F., dal Fiume D., Morelli E., Spada G., 1985, *ApJ*, 298, 585
- Habets G. M. H. J., Heintze J. R. W., 1981, *A&AS*, 46, 193
- Hill A. B. et al., 2005, *A&A*, 439, 255
- Ibragimov A., Kajava J. J. E., Poutanen J., 2011, *MNRAS*, 415, 1864
- Jenke P. A., Finger M. H., Wilson-Hodge C. A., Camero-Arranz A., 2012, *ApJ*, 759, 124
- Koyama K. et al., 2007, *PASJ*, 59, 23
- Lutovinov A., Revnivtsev M., Gilfanov M., Shtykovskiy P., Molkov S., Sunyaev R., 2005, *A&A*, 444, 821
- Mason A. B., Clark J. S., Norton A. J., Crowther P. A., Tauris T. M., Langer N., Neugeruela I., Roche P., 2012, *MNRAS*, 422, 199
- Mihara T., 1995, PhD thesis, Department of Physics, Univ. Tokyo
- Nagase F., 1989, *PASJ*, 41, 1
- Naik S., Paul B., Callanan P. J., 2005, *ApJ*, 618, 866
- Naik S., Maitra C., Jaisawal G. K., Paul B., 2013, *ApJ*, 764, 158
- Pradhan P., Maitra C., Paul B., Islam N., Paul B. C., 2014, *MNRAS*, 442, 2691
- Pravdo S. H., Becker R. H., Boldt E. A., Holt S. S., Serlemitsos P. J., Swank J. H., 1976, *BAAS*, 8, 512
- Rappaport S. A., Joss P. C., 1983, in Lewin W. H. G., van den Heuvel E. P. J., eds, *Accretion-Driven Stellar X-ray Sources*. Cambridge Univ. Press, Cambridge, p. 13
- Rubin B. C. et al., 1996, *ApJ*, 459, 259
- Sugizaki M., Mitsuda K., Kaneda H., Matsuzaki K., Yamauchi S., Koyama K., 2001, *ApJS*, 134, 77
- Takahashi T. et al., 2007, *PASJ*, 59, 35
- Tanaka Y., 1986, in Mihalas D., Winkler K.-H. A., eds, *Lecture Notes in Physics Vol. 255, IAU Colloq. 89, Radiation Hydrodynamics in Stars and Compact Objects*. Springer Verlag, Berlin, p. 198
- Thompson T. W. J., Tomsick J. A., Rothschild R. E., in't Zand J. J. M., Walter R., 2006, *ApJ*, 649, 373
- van Kerkwijk M. H., van Paradijs J., Zuiderwijk E. J., 1995, *A&A*, 303, 497
- White N. E., Swank J. H., Holt S. S., 1983, *ApJ*, 270, 711

This paper has been typeset from a $\text{\TeX}/\text{\LaTeX}$ file prepared by the author.